



Direct evidence of gradient Mn(II) evolution at charged states in $\text{LiNi}_{0.5}\text{Mn}_{1.5}\text{O}_4$ electrodes with capacity fading



Ruimin Qiao ^{a,1}, Yuesheng Wang ^{b,1}, Paul Olalde-Velasco ^{a,2}, Hong Li ^b, Yong-Sheng Hu ^{b,*,**}, Wanli Yang ^{a,*}

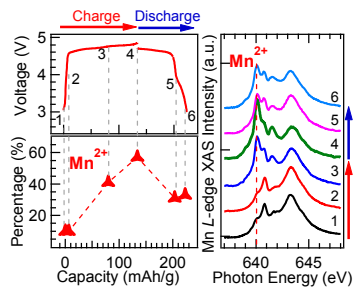
^a Advanced Light Source, Lawrence Berkeley National Laboratory, Berkeley, CA 94720, USA

^b Institute of Physics, Chinese Academy of Sciences, Beijing 100190, PR China

HIGHLIGHTS

- Soft X-ray spectroscopy confirms the direct link between Mn^{2+} and capacity fading.
- Mn^{2+} is formed mainly at charged states, contradicting disproportional reaction scenario.
- Mn^{2+} formation is mostly on the side of the electrodes facing electrolyte separator.
- The surface reaction is critical for understanding and optimizing battery electrodes.

GRAPHICAL ABSTRACT



ARTICLE INFO

Article history:

Received 20 July 2014

Received in revised form

24 September 2014

Accepted 2 October 2014

Available online 13 October 2014

Keywords:

$\text{LiNi}_{0.5}\text{Mn}_{1.5}\text{O}_4$

Lithium ion battery

Electrolyte degradation

Manganese dissolution

Soft X-ray absorption spectroscopy

ABSTRACT

Mn evolution has long been considered critical for understanding the capacity fading of spinel electrodes in batteries. However, the detailed mechanism is still under debate; chemical evolution and distribution of the detrimental Mn is yet to be experimentally clarified. Here we perform a comparative soft X-ray absorption spectroscopic study on two batches of $\text{LiNi}_{0.5}\text{Mn}_{1.5}\text{O}_4$ with the same bulk spinel phase, but different electrochemical performance. By virtue of the sensitivity of soft X-ray to the transition-metal 3d states and oxygen 2p states, evolutions of Ni, Mn, and O in $\text{LiNi}_{0.5}\text{Mn}_{1.5}\text{O}_4$ are compared between the two batches of electrodes. In the $\text{LiNi}_{0.5}\text{Mn}_{1.5}\text{O}_4$ with fast capacity fading, Mn^{2+} is evidently observed in the initial charge cycle. Strikingly, the Mn^{2+} content is notably high at the fully charged state. This sharply contradicts the conventional wisdom that Mn^{2+} evolves from a disproportional reaction favored in the discharged state. Additionally, the shallow probe depth of soft X-ray spectroscopy enables another finding that Mn^{2+} manifests itself mostly on the side of the electrode facing separator. Our comparative study provides direct experimental evidence on the association between Mn^{2+} and performance failure. It strongly suggests that Mn^{2+} formation is mostly determined by electrode-electrolyte surface reactions, instead of disproportional reactions.

© 2014 Elsevier B.V. All rights reserved.

1. Introduction

Developing positive electrodes with high energy density is one of the crucial challenges for employing lithium-ion batteries for electric vehicles and other sustainable energy applications [1–4]. Among all the positive electrode materials, $\text{LiNi}_{0.5}\text{Mn}_{1.5}\text{O}_4$ (LNMO)

* Corresponding author.

** Corresponding author.

E-mail addresses: yshu@aphy.iphy.ac.cn (Y.-S. Hu), wlyang@lbl.gov (W. Yang).

1 Both authors contributed equally to this work.

2 Present address: Paul Scherrer Institute, 5232 Villigen PSI, Switzerland.

has attracted much attention due to its low-cost, non-toxicity, good rate capability, and especially, high operation voltage [5–8]. With a high operating voltage (4.7 V) and a practical capacity (130 mAh g⁻¹) comparable to that of LiCoO₂ (4.2 V; 140 mAh g⁻¹) and LiFePO₄ (3.4 V; 160 mAh g⁻¹), LNMO provides a specific energy higher than all currently commercialized compounds [8]. Moreover, the high voltage provides room for negative electrodes that perform better than carbon. For example, the combination of LiNi_{0.5}Mn_{1.5}O₄ cathode with Li₄Ti₅O₁₂ anode (1.55 V), both in spinel structure, enables a 3 V lithium-ion battery with high power capability [9,10], and perfect cyclability if the capacity limit is set by Li₄Ti₅O₁₂ anode [11]. However, several critical issues, in particular, electrolyte degradation at the high voltage and transition metal (TM), especially Mn, dissolution, need to be solved before LNMO could be implemented in a commercial battery cell [12–16].

In conventional wisdom, the electrolyte degradation and Mn dissolution are generally considered two isolated issues. Electrolyte degradation in high-voltage battery cells stems from the high energy level of the electrolyte's highest occupied molecular orbital (HOMO). The electrolyte will be oxidized by electron charge transfer from its HOMO to the high-voltage (low-energy level) positive electrodes [3]. Mn dissolution is widely believed to be from Mn²⁺ species that are generated from the disproportional reaction of 2Mn³⁺ → Mn⁴⁺ + Mn²⁺. Naturally, such mechanism is enhanced or requires lower Mn valence at discharged state. As a matter of fact, cation doping of LiMn₂O₄ spinel material with divalent Ni is based on the same consideration. Ideally, the stoichiometric LiNi_{0.5}Mn_{1.5}O₄ contains only Mn⁴⁺ and the redox process occurs on the Ni site only, which was expected to prevent the creation of the Mn³⁺ cation and its related problem, such as Jahn–Teller distortion and disproportional reaction associated with Mn dissolution [17,18]. It is proposed that the Mn⁴⁺ of the LiNi_{0.5}Mn_{1.5}O₄ spinel, lowers both the Ni³⁺/Ni²⁺ couple to 4.7 V and the top of the O-2p bands to 4.8 V to enable a high-voltage operation based on Ni³⁺/Ni²⁺ and Ni⁴⁺/Ni³⁺ couples with no significant voltage step between them [8,19–22].

However, Mn³⁺ has been observed in LNMO positive electrodes [23–26], and studies have shown that LNMO still suffers severe Mn dissolution problem [13,14,27,28]. Contrary to the conventional wisdom, Pieczonka et al. have found that the amount of dissolved TMs actually increases with the state-of-charge (SOC), i.e., dissolution is enhanced at the charged state, not the discharged state with generally low TM valences [13]. The same phenomenon has also been observed in LiMn₂O₄ spinel [29,30]. In particular, Jang etc. found an intriguing relationship between surface area and dissolution effect [30]. These works question our conventional understanding of the isolated electrolyte instability and TM dissolution problems, strongly suggest the association between the two phenomena, and indicate the critical role of surface reactions for truly understand the performance issues in high-voltage materials.

In this work, we aim to provide direct experimental evidences to confirm the detrimental effect of Mn²⁺ as the ringleader of performance decay in LNMO positive electrodes, and to provide a valence-sensitive and side-sensitive study of the electrode surface reactions. In order to circumvent the complicated factors arising from LNMO in different phases [31], we elaborately studied two different LNMO materials with the same sintering condition, but different gaseous environments during the final cooling process. All LNMO samples exhibit *Fd-3m* bulk structure, which is preferred for electrochemical cycling [19]. But samples cooled in air display much more serious capacity fading compared with those quenched in N₂. While the Ni and O seem to behave similarly in the two systems, soft X-ray absorption spectroscopy (sxAS) reveals strong surface reaction involving Mn²⁺ in samples with severe capacity fading. Mn²⁺ is unambiguously resolved on the side of the

electrode facing electrolyte separator, but remains weak on the side facing current collector. Strikingly, the intensity of Mn²⁺ is much stronger at the charged states, compared with that at discharged states. Our results provide direct valence-sensitive evidence of the link between Mn²⁺ evolution and performance failure. It also supports the scenario that Mn²⁺ evolution stems from surface reactions with electrolyte, instead of disproportional reactions.

2. Experimental

2.1. LiNi_{0.5}Mn_{1.5}O₄ sample preparation

LiNi_{0.5}Mn_{1.5}O₄ samples were prepared by solid state reaction. Stoichiometric amounts of lithium carbonate (Li₂CO₃, AR, 99%, Alfa), manganese nitrates (Mn(NO₃)₂·4H₂O, AR, 98%, Alfa) and nickel nitrates (Ni(NO₃)₂·6H₂O, AR, 98%, Alfa) are dissolved in ethanol. Then, after evaporation of the solvent under continuously stirring at 80 °C, the resulting paste is pre-heated at 500 °C for 2 h, and further sintered at 800 °C for 8 h. All the preheating and sintering processes are taken in ambient atmosphere. The as-sintered samples are cooled down in two different processes: some are quenched in N₂ with the cooling rate more than 50 °C min⁻¹, others are cooled gradually in air at 1 °C min⁻¹.

2.2. Electrochemical test

LiNi_{0.5}Mn_{1.5}O₄ as active material is mixed with acetylene black and polyvinyl difluoride (PVDF) in 1-methyl-2-pyrrolidone (NMP) with a weight ratio of 85:10:5 to form slurry. The slurry is then coated onto a roughened aluminum current collector using a doctor blade. The composite electrode has a thickness of 50 μm. Subsequently, a cell is assembled using LiNi_{0.5}Mn_{1.5}O₄ as the cathode, Li as the anode, and glass fiber as the separator in a glove box with Ar atmosphere. 1 M LiPF₆ in ethylene carbonate/diethylcarbonate (EC/DEC) by volume (1:2) is used as the electrolyte in the experiments. The cells are cycled at room temperature (25 °C) between 4.9 and 3 V vs. Li⁺/Li under the constant current rate of 10 mA g⁻¹. Charge–discharge capacities are calculated with respect to the mass of LiNi_{0.5}Mn_{1.5}O₄.

2.3. Soft X-ray spectroscopy

sXAS was performed at Beamline 8.0.1 of the Advanced Light Source (ALS) at Lawrence Berkeley National Laboratory (LBNL). The undulator and spherical grating monochromator supply a linearly polarized photon beam with resolving power up to 6000 [32]. The experimental energy resolution is 0.1–0.15 eV. Data were collected in both total electron yield (TEY) and total fluorescence yield (TFY) modes simultaneously, corresponding to probe depth of about 10 nm (for TEY) and 100 nm (for TFY). All the spectra have been normalized to the beam flux measured by the upstream gold mesh.

3. Results and discussions

LiNi_{0.5}Mn_{1.5}O₄ samples were prepared by solid state reaction. The as-sintered samples are cooled down in two different processes: some are quenched in N₂, denoted as N₂-quenched samples hereafter, others are cooled gradually in air at 1 °C min⁻¹, denoted as air-cooled samples hereafter. The structural and electrochemical properties of the LiNi_{0.5}Mn_{1.5}O₄ materials prepared with different cooling processes are compared in Fig. 1. Fig. 1(a) shows similar XRD patterns of both N₂-quenched and air-cooled samples. Except for a trace amount of Li_xNi_yO, all peaks in XRD can be indexed by spinel structures with a space group of *Fd-3m* (JCPDS Card No.: 01-080-2162), indicating both samples are dominated by the Ni/Mn

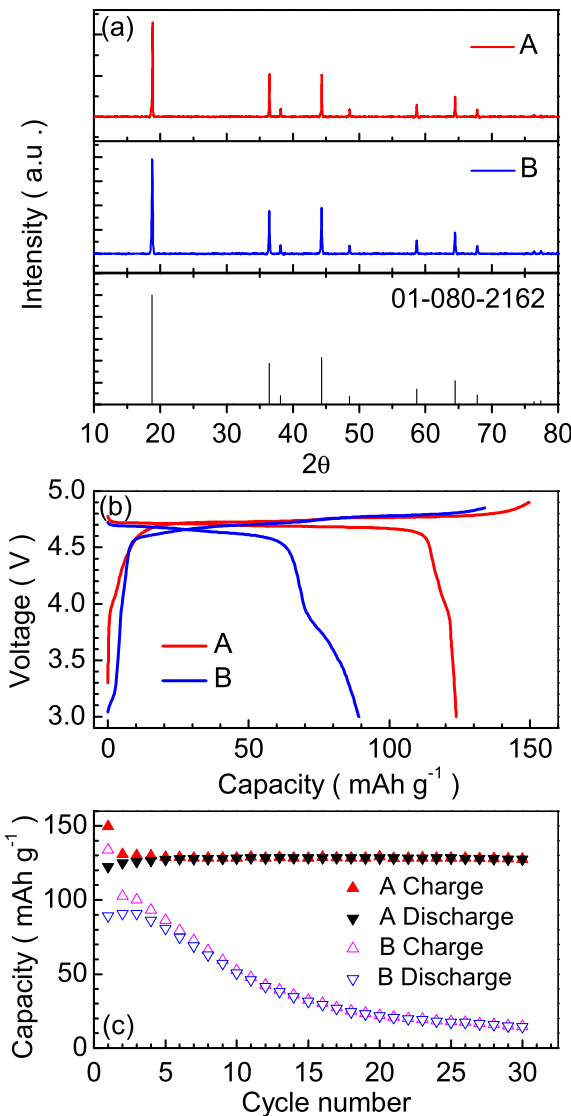


Fig. 1. Structural and electrochemical properties of $\text{LiNi}_{0.5}\text{Mn}_{1.5}\text{O}_4$ materials prepared with two different cooling processes, i.e., quenched in N_2 (A) and gradually cooled in air (B). (a) Both batches of samples show similar XRD patterns, indicating both are $Fd\text{-}3m$ phase (JCPDS data No. 01-080-2162) in bulk. (b) Charge/discharge curves during the first cycle. (c) Charge/discharge capacity as a function of cycle number.

disordered $Fd\text{-}3m$ phase in bulk [33]. Despite of the similar phase in bulk, dramatically different electrochemical properties are observed. As shown in Fig. 1(b) and (c), the N_2 -quenched material (A) displays a discharge capacity of 122.5 mAh g^{-1} and a Coulombic efficiency of 82% during the initial cycling. In the subsequent several cycles, its discharge capacity increases slightly to 127.5 mAh g^{-1} and is stabilized until 30 cycles where the test is ended. In sharp contrast, the air-cooled material (B) exhibits much lower initial discharge capacity (89 mAh g^{-1}) and Coulombic efficiency (66%). B also displays significant capacity fading (only 14 mAh g^{-1} at the 30th cycle). The different electrochemical performance between the N_2 -quenched and air-cooled materials could be attributed to many factors [5], for example, particle morphology [34,35], preferential orientation [36], size [20,26], surface area [37] and oxygen deficiency [5,23,35]. Nevertheless, these two batches of spinel LNMO samples are perfect candidates for a comparative study on the critical surface reaction associated with capacity fading.

sXAS measurements of Ni, Mn L -edges and O K -edge are conducted on a series of $\text{LiNi}_{0.5}\text{Mn}_{1.5}\text{O}_4$ electrodes that are electrochemically cycled to the desired SOC. All electrodes are vigorously rinsed with DMC and dried in Ar glove box immediately after cell disassembly to lock the SOC. Exposed electrodes are transferred into ultra-high vacuum sXAS endstation through our special sample transfer kit to avoid any air exposure [38]. Ni-, Mn- $3d$ and O- $2p$ states of $\text{LiNi}_{0.5}\text{Mn}_{1.5}\text{O}_4$ are directly probed through dipole-allowed TM- L and O- K edges [38–42]. Taking advantage of the shallow probe depth (<200 nm) of soft X-rays, we are able to detect the reactions on different sides of the electrodes, i.e., the side facing current collectors and facing separators.

Fig. 2 shows the TM- L edge sXAS spectra and simulation results of their valence evolution in N_2 -quenched LNMO. Data are collected on the electrode side facing separators. The voltage profile is typical for the disordered phase [19], which displays the predominant plateau at 4.7 V and a small plateau at approximately 4.1 V contributing to only about 10% of the total capacity. For this study, six N_2 -quenched $\text{LiNi}_{0.5}\text{Mn}_{1.5}\text{O}_4$ cells with the same configuration were electrochemically cycled under the same condition to different states (Table S1), which are marked on the voltage profiles shown in Fig. 2(a).

In Fig. 2(b), (c) and (d), both Mn and Ni L -edge sXAS spectra consist of well-separated L_2 and L_3 absorption features, resulting from the $2p$ core-hole spin-orbital splitting [39]. For Mn L -edge sXAS, TEY spectra are shown in main text, with TFY in supplementary (Fig. S1). TFY lineshape is severely distorted by the self-absorption effect and do not represent the absorption cross-section on Mn L -edge [43]. The absorption profile of both Mn- L and Ni- L sXAS evolves reversibly during the charge and discharge process, indicating reversible redox reaction on both Mn and Ni sites. Below we elaborate this reversible Mn and Ni redox through quantitative fitting and qualitative lineshape analysis.

For Mn- L sXAS data, reference spectra collected on MnO (Mn^{2+}), Mn_2O_3 (Mn^{3+}) and Li_2MnO_3 (Mn^{4+}) display dramatically different absorption profiles. We have shown before that manganese compounds with Mn occupying an octahedral site exhibit similar Mn- L absorption profiles for the same Mn valences, despite different ligands and crystal structures in different systems [42]. This allows us to quantitatively analyze the evolution of the concentration of Mn^{4+} , Mn^{3+} and Mn^{2+} through simple simulations based on linear combination of the reference spectra. The simulated spectra are plotted as dotted lines in Fig. 2(b) with great agreement with experimental data (solid lines), and the results on Mn valence are plotted in Fig. 2(e). In all N_2 -quenched samples, the amount of Mn^{2+} is negligible. The pristine electrode (#1) contains about 20% Mn^{3+} and 80% Mn^{4+} . Most of the Mn^{3+} is oxidized to Mn^{4+} when the material is half charged (#3) and stays at Mn^{4+} . Reversed process is observed during discharge, from #5 to #6 around the 4.1 V plateau. This directly proves the 4.1 V plateau is associated with $\text{Mn}^{3+}/\text{Mn}^{4+}$ redox couple. The fully discharged sample (#6) shows slightly higher Mn^{3+} than the pristine one (#1), which might be responsible for the low Coulombic efficiency of the material during the initial cycle.

On the Ni L -edge sXAS data (Fig. 2(c) and (d)), the intensity ratio of the two peaks in the Ni- L_3 region, marked as A and B, fingerprints the oxidation states of Ni [41,44], which changes from Ni^{2+} to Ni^{4+} during charge process (#1–#4), and vice versa during discharge (#4–#6) (Fig. 2(f)). From half charge (#3) to fully charge (#4), $\text{Ni}^{4+}/\text{Ni}^{2+}$ intensity ratio increase while Mn stays at Mn^{4+} , suggesting the plateau at around 4.7 V is due to the $\text{Ni}^{2+}/\text{Ni}^{4+}$ redox. Note that the surface-sensitive TEY signal is consistent with the bulk-sensitive TFY data in the trend of lineshape changes, but shows lower Ni oxidation states. Moreover, the Ni oxidation state here is much lower than that in the $\text{LiCo}_{0.33}\text{Ni}_{0.33}\text{Mn}_{0.33}\text{O}_2$ case [41], which might

be related with the Ni^{2+} dissolution problem in $\text{LiNi}_{0.5}\text{Mn}_{1.5}\text{O}_4$ [13,14].

Fig. 3 shows the Mn *L*-edge sXAS collected on both electrode sides facing separator (a) and current collector (b) of another batch of N_2 -quenched LMNO. No essential difference is found between two sets of Mn-*L* data. The Ni-*L* and O-*K* sXAS spectra show no gradient effect from the current collector side to the separator side either (**Figs. S2–S5**).

Compared with N_2 -quenched LNMO samples, sXAS data collected on air-cooled samples display very different TM-*L* spectral evolution. Samples with different SOC are marked in **Fig. 4(a)** (**Table S1**). **Fig. 4(b)** and (c) plots the Ni *L*-edge TEY and TFY sXAS spectra collected on the facing separator side. Generally, the Ni-*L* spectral evolution of the air-cooled samples resembles that of the N_2 -quenched samples (**Fig. 2**). However, the B/A ratio in the fully charged state (#4) of the air-cooled sample is much weaker than that in the N_2 -quenched ones, especially for TEY signals, suggesting less Ni^{2+} is oxidized to Ni^{4+} in the air-cooled samples. This is consistent with the much reduced capacity of the material. Same as the N_2 -quenched samples, the Ni-*L* sXAS spectra collected on the side of the electrode facing current collector (**Fig. S5**) show no difference with those collected on the side facing separator. This is in sharp contrast to the gradient behavior of Mn across the electrodes, which is discussed below.

Fig. 5 shows the central results of this paper. Mn *L*-edge sXAS of samples with different SOC (TEY in **Fig. 5(a)** and TFY in **Fig. S6**) display distinctly different spectra collected on the sides of the electrodes facing separator (b) and current collector (c). The absorption profiles of the Mn-*L* spectra are significantly different from that of the N_2 -quenched samples (**Fig. 3**). In **Fig. 5(b)**, the sharp and strong sXAS peak at 640 eV suggests significant amount of Mn^{2+} evolves from the very first charge cycle. Surprisingly, such strong Mn^{2+} features do not manifest on the side facing current collector. The simulated spectra using linear combination of the Mn^{2+} , Mn^{3+} and Mn^{4+} reference spectra are shown in dashed lines. The deduced values of the concentrations of Mn^{2+} , Mn^{3+} and Mn^{4+} (**Fig. 5(d)–(f)**) show quantitatively the evolution of different Mn valence with electrochemical cycling. Mn^{2+} starts to evolve during the first charge process, and reaches the maximum of almost 60% at the fully charged state (#4) on the side of the electrode facing separator.

The significant amount of Mn^{2+} at charged states of the air-cooled samples is also confirmed by both the TEY and TFY data of O-*K* spectra (**Fig. 6** and **Supplementary Figs. S7–S8**). Besides the broad humps of O-*K* spectra above 534 eV, which are associated with the transitions from O-1s to O-2p and hybridized Mn-4s, *p* orbitals, the pre-edge peaks between 528 and 531 eV correspond to the hybridized states of Mn-3d and O-2p. These pre-edge features

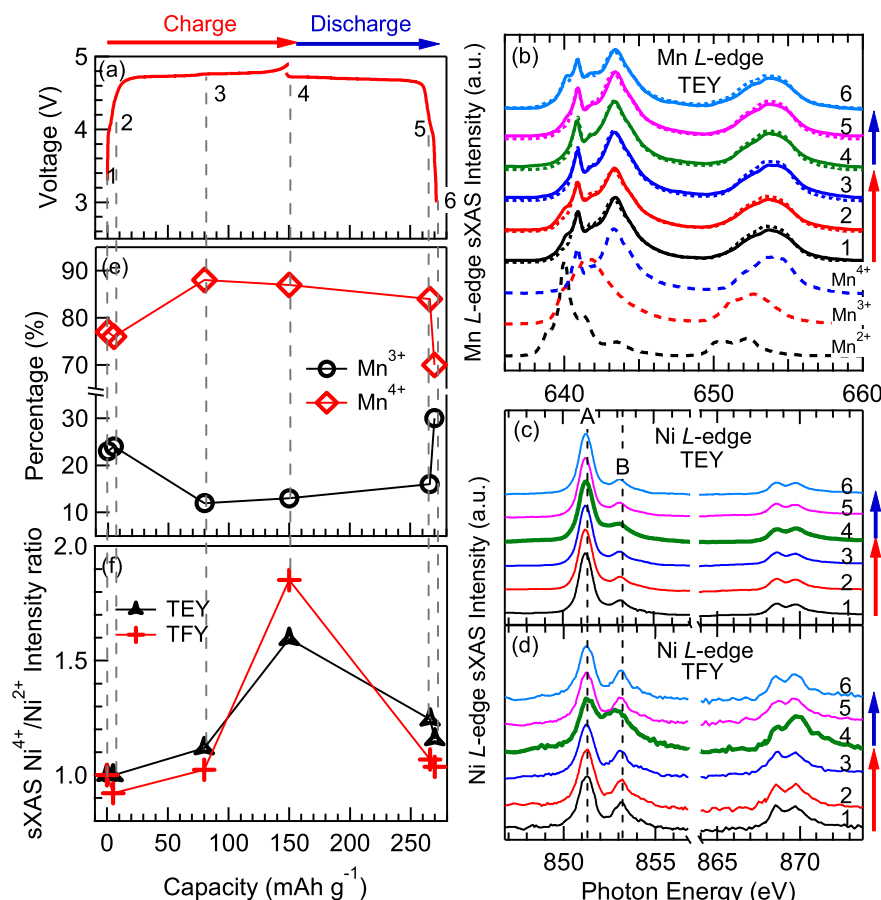


Fig. 2. Evolution of the chemical valence of the transition metal elements in N_2 -quenched samples. (a) The measured electrodes with different SOC are marked on the voltage profiles. (b) Mn *L*-edge sXAS spectra (TEY) collected on the $\text{LiNi}_{0.5}\text{Mn}_{1.5}\text{O}_4$ electrode samples (solid lines) and references (dash lines) with different formal Mn valences, including MnO (Mn^{2+}), Mn_2O_3 (Mn^{3+}) and Li_2MnO_3 (Mn^{4+}). Dotted lines on top of the sXAS spectra are simulation results by linearly combining Mn^{3+} and Mn^{4+} spectra. (c) and (d) Ni *L*-edge sXAS spectra collected in both TEY and TFY mode, respectively. (e) Quantitative values of Mn^{3+} and Mn^{4+} concentration as a function of the electrochemical cycling status. (f) The intensity ratio of the absorption features B to A on the Ni-*L* sXAS spectra (c and d), which qualitatively corresponds to the $\text{Ni}^{4+}/\text{Ni}^{2+}$ ratio. The values are all normalized to the ratio in the pristine sample (#1).

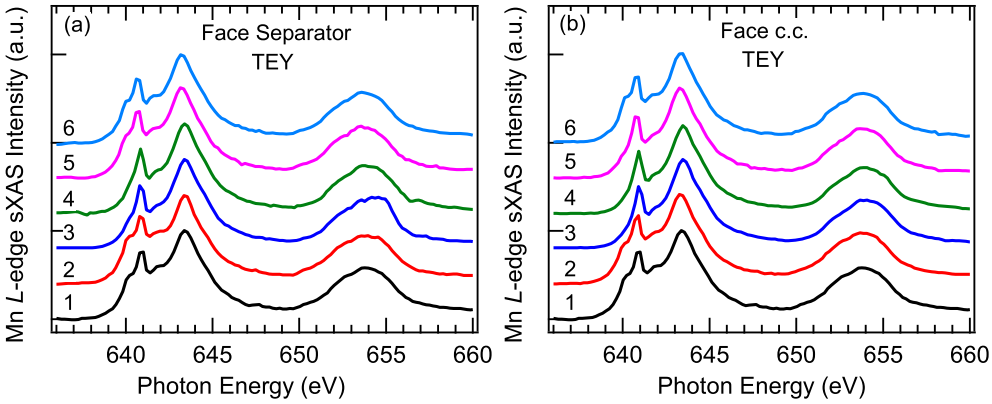


Fig. 3. Mn L -edge sXAS spectra, collected on the facing separator (a) and current collector (b) sides of N_2 quenched LMNO electrodes. Sample numbers follows the same definition as in Fig. 2(a).

in the O K -edge sXAS spectra provide important information about the chemical bonding between O and Mn [42,45]. For N_2 -quenched samples, the changes in the O K -edge sXAS spectra during charge/discharge process are relatively small, which is similar to that observed in $LiMn_2O_4$ involving only Mn^{3+} and Mn^{4+} [46]. In contrast, for air-cooled samples, the intensity of the pre-edge features dramatically decreases at charged states (#4). This is consistent with the existence of the considerable amount of Mn^{2+} at charged states, because Mn^{2+} species feature much reduced O- K hybridization intensity due to the exchange stability effect [42].

Several important conclusions could be drawn based on the spectroscopic observation of the Mn^{2+} evolution. Firstly, XRD indicates both N_2 -quenched and air-cooled samples are dominated by the disordered $Fd\text{-}3m$ phase in bulk (Fig. 1). Also, both pristine electrodes display about 80% Mn^{4+} (Figs. 2 and 5). However, air-cooled samples show much more severe capacity fading in electrochemical cycling, with considerable amount of Mn^{2+} evolving

during the initial charge process. The Mn^{2+} concentration in the fully charged sample (#4) reaches 60% on the side of the electrode facing separator (Fig. 5). This is in sharp contrast to the N_2 -quenched sample, where only Mn^{4+} is observed in charged states. Although sample A shows little capacity fading in the first 30 cycles, we assume the failing mechanism from Mn^{2+} formation is universal based on extensive reports in literature [47]. The comparison of the Mn sXAS results on sample A and B in the initial cycle provides a direct experimental evidence on the detrimental effects of surface Mn^{2+} on electrochemical performance.

Secondly, majority of the Mn^{2+} evolves on the side of the electrode facing separator, not the side facing current collector (Fig. 5). Although electrolyte typically soaks into composite electrodes, the side of the electrodes facing current collectors is exposed by peeling off the electrode laminate from current collector. TEY of sXAS only detects the 10 nm layer on the exposed electrode surfaces, which is the portion of the electrode with minimum electrolyte access. The

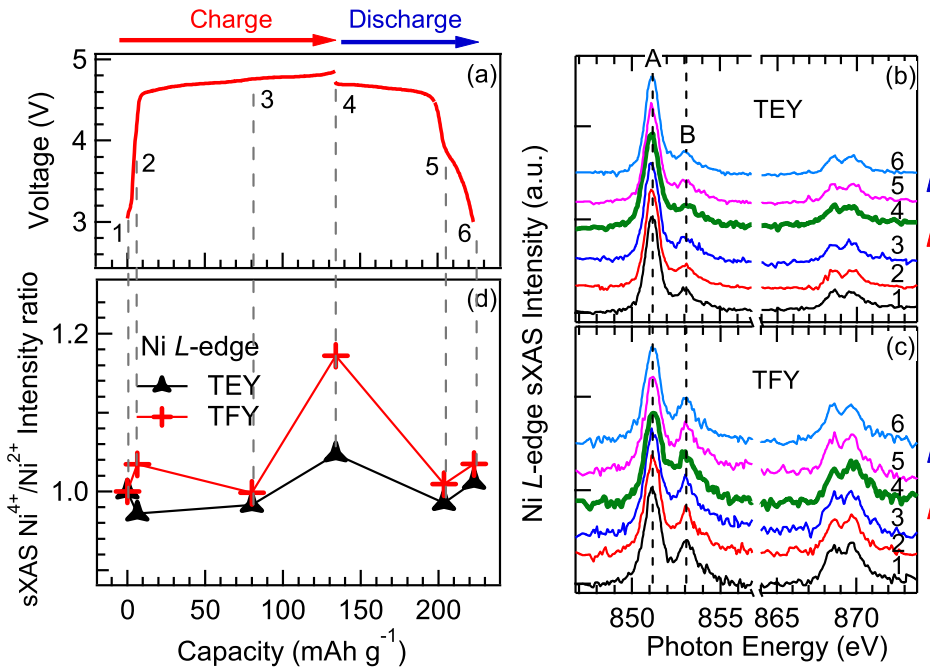


Fig. 4. Evolution of the Ni valence in air-cooled LNMO samples. (a) The electrodes with different SOC used for sXAS measurements are marked on the voltage profiles. (b) and (c) Ni L -edge sXAS spectra collected in TEY and TTFY modes. (d) The sXAS intensity ratio of the absorption features B to A marked on the Ni- L sXAS spectra in (b) and (c). Values are normalized to that of the pristine sample (#1).

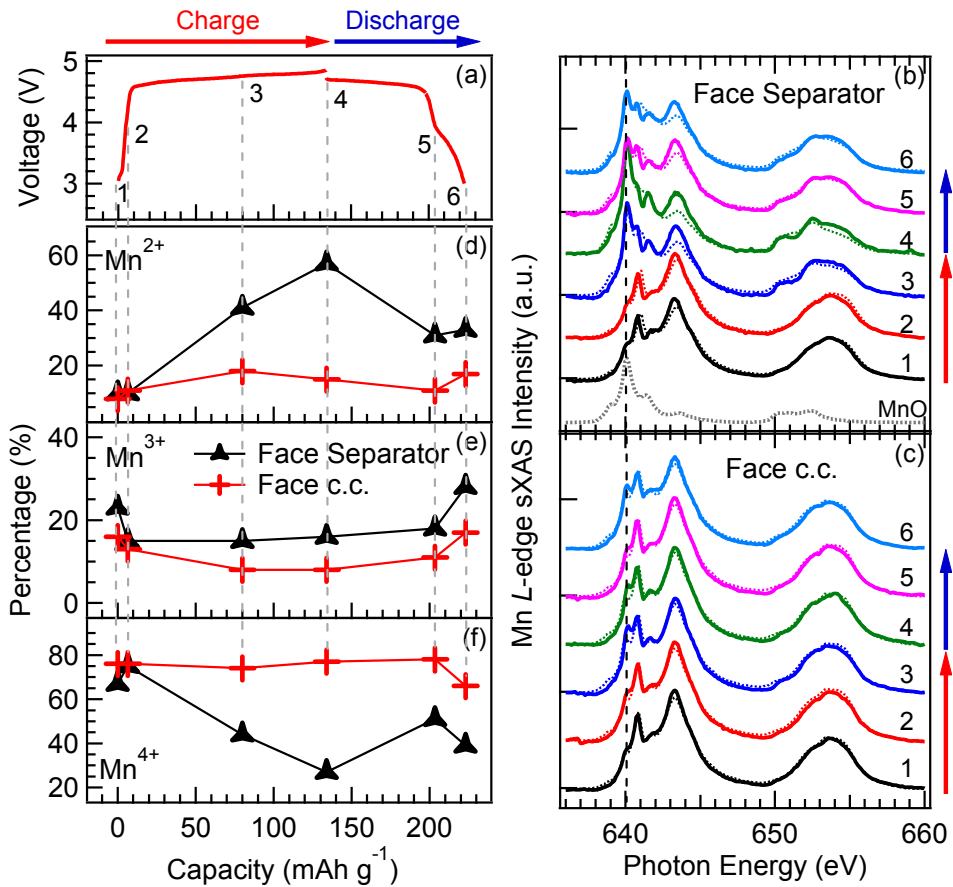


Fig. 5. Evolution of the chemical valence of Mn in electrodes based on air-cooled LNMO. (a) The electrodes with different SOC used for sXAS measurements are marked on the voltage profiles. (b) and (c) Mn *L*-edge sXAS spectra (TEY) collected on the sides of electrodes facing separator (b) and current collector (c). Dotted lines on top of the spectra are simulated results for obtaining the quantitative values of Mn²⁺, Mn³⁺ and Mn⁴⁺ concentration. (d), (e) and (f) Evolution of the Mn valence deduced from spectral simulations, with respect to the charge/discharge states.

sharp contrast of Mn²⁺ concentration on the two sides of the electrodes suggests the critical role of the electrolyte in the formation of Mn²⁺ [48–51].

Thirdly, our data show clearly that Mn²⁺ forms during the very first charging process. The amount of Mn²⁺ reaches maximum in charged states (#3 and #4), and decreases in the further discharged states (#5 and #6). This contradicts the common belief that Mn²⁺ evolves from disproportional reaction, which supposes to be

enhanced at discharged states with low Mn valence. This observation is consistent with the recent report on enhanced Mn dissolution from charged LMNO electrodes, where catalytic effect of Mn⁴⁺ species at charged state is considered to promote the electrolyte decomposition [13]. As elaborated above, Mn²⁺ mainly forms on the side of the electrode facing electrolyte separator, which indicates that electrolyte degradation plays a critical role on the reduction and dissolution of Mn at high voltage, i.e., charged

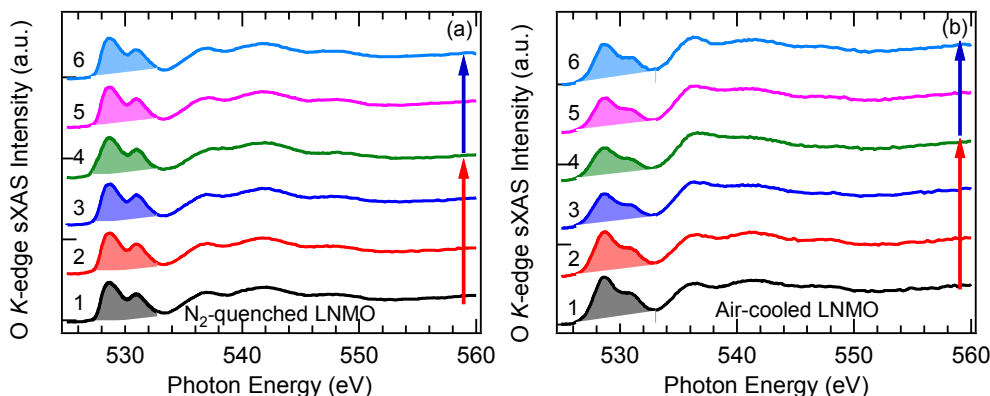


Fig. 6. O *K*-edge sXAS spectra (TFY) of N₂-quenched (a) and air-cooled (b) samples. The spectra were collected on the side of electrodes facing separator. Sample numbers follows the same definition as in Figs. 2(a) and 4(a). TEY data and spectra collected on the other side of the electrodes are displayed in Supplementary Figs. S7–S8.

states. Therefore, our results support the scenario of Mn²⁺ formation associated with electrolyte degradation: the catalytic effect of Mn⁴⁺ species at charged state leads to severe electrolyte degradation; conversely, the interface of the decomposed electrolyte influences (reduces) the Mn on the surface, forming large amount of Mn²⁺ on the surface at charged states.

4. Conclusions

In summary, we provide valence-sensitive and side-sensitive sXAS studies of the Mn, Ni, O evolution in two different LNMO electrodes based on N₂-quenched and air-cooled materials. The later shows significant capacity fading in electrochemical cycling despite of their identical bulk phase tested by X-ray diffraction patterns. The sXAS confirms that the small 4.1 V plateau arises from Mn³⁺/Mn⁴⁺ redox couple, and the predominant 4.7 V plateau is from the Ni²⁺/Ni⁴⁺ redox. Comparison of the Mn-L, Ni-L, and O-K sXAS results directly show that the poor electrochemical performance of the air-cooled samples stems from considerable amount of Mn²⁺ formation. Strikingly, the Mn²⁺ concentration is found to be notably high on the surface at the charged state where Mn⁴⁺ was generally expected, and it evolves clearly on the side of the electrode facing battery separators. Our result questions the conventional wisdom that Mn²⁺ evolves from disproportional reactions, and strongly suggests that electrolyte degradation and Mn dissolution are two correlated issues of LNMO based high-voltage electrodes, which may stimulate each other at the high voltage (charged) states through surface catalytic effect of the high-valence Mn species [13,29,30].

Acknowledgments

The Advanced Light Source is supported by the Director, Office of Science, Office of Basic Energy Sciences, of the U.S. Department of Energy under Contract No. DE-AC02-05CH11231. This work was partly supported by funding from "973" Projects (2010CB833102, 2012CB932900), NSFC (No. 51222210), and the 100 Talent Project of the Chinese Academy of Sciences.

Appendix A. Supplementary data

Supplementary data related to this article can be found at <http://dx.doi.org/10.1016/j.jpowsour.2014.10.013>.

References

- [1] J.M. Tarascon, M. Armand, *Nature* 414 (2001) 359–367.
- [2] M.S. Whittingham, *Chem. Rev.* 104 (2004) 4271–4302.
- [3] J.B. Goodenough, Y. Kim, *Chem. Mater.* 22 (2009) 587–603.
- [4] B.L. Ellis, K.T. Lee, L.F. Nazar, *Chem. Mater.* 22 (2010) 691–714.
- [5] Q. Zhong, A. Bonakdarpour, M. Zhang, Y. Gao, J.R. Dahn, *J. Electrochem. Soc.* 144 (1997) 205–213.
- [6] R. Santhanam, B. Rambabu, *J. Power Sources* 195 (2010) 5442–5451.
- [7] J. Hassoun, K.-S. Lee, Y.-K. Sun, B. Scrosati, *J. Am. Chem. Soc.* 133 (2011) 3139–3143.
- [8] D. Liu, W. Zhu, J. Trottier, C. Gagnon, F. Baray, A. Guerfi, A. Mauger, H. Grout, C.M. Julien, J.B. Goodenough, K. Zaghib, *RSC Adv.* 4 (2014) 154–167.
- [9] R. Dedryvère, D. Foix, S. Franger, S. Patoux, L. Daniel, D. Gonbeau, *J. Phys. Chem. C* 114 (2010) 10999–11008.
- [10] H.-G. Jung, M.W. Jang, J. Hassoun, Y.-K. Sun, B. Scrosati, *Nat. Commun.* 2 (2011) 516.
- [11] H.F. Xiang, X. Zhang, Q.Y. Jin, C.P. Zhang, C.H. Chen, X.W. Ge, *J. Power Sources* 183 (2008) 355–360.
- [12] A. von Cresce, K. Xu, *J. Electrochem. Soc.* 158 (2011) A337–A342.
- [13] N.P.W. Pieczonka, Z. Liu, P. Lu, K.L. Olson, J. Moote, B.R. Powell, J.-H. Kim, *J. Phys. Chem. C* 117 (2013) 15947–15957.
- [14] N.S. Norberg, S.F. Lux, R. Kostecki, *Electrochim. Commun.* 34 (2013) 29–32.
- [15] C. Delacourt, A. Kwong, X. Liu, R. Qiao, W.L. Yang, P. Lu, S.J. Harris, V. Srinivasan, *J. Electrochem. Soc.* 160 (2013) A1099–A1107.
- [16] S. Komaba, N. Kumagai, Y. Kataoka, *Electrochim. Acta* 47 (2002) 1229–1239.
- [17] G.G. Amatucci, N. Pereira, T. Zheng, J.-M. Tarascon, *J. Electrochem. Soc.* 148 (2001) A171–A182.
- [18] J.C. Hunter, *J. Solid State Chem.* 39 (1981) 142–147.
- [19] J.H. Kim, S.T. Myung, C.S. Yoon, S.G. Kang, Y.K. Sun, *Chem. Mater.* 16 (2004) 906–914.
- [20] X. Ma, B. Kang, G. Ceder, *J. Electrochem. Soc.* 157 (2010) A925–A931.
- [21] E. Lee, K.A. Persson, *Energy Environ. Sci.* 5 (2012) 6047–6051.
- [22] L. Wang, H. Li, X. Huang, E. Baudrin, *Solid State Ionics* 193 (2011) 32–38.
- [23] J. Xiao, X. Chen, P.V. Sushko, M.L. Sushko, L. Kovarik, J. Feng, Z. Deng, J. Zheng, G.L. Graff, Z. Nie, D. Choi, J. Liu, J.-G. Zhang, M.S. Whittingham, *Adv. Mater.* 24 (2012) 2109–2116.
- [24] K.M. Shaju, P.G. Bruce, *Dalton Trans.* (2008) 5471–5475.
- [25] J. Cabana, M. Casas-Cabanas, F.O. Omenya, N.A. Chernova, D. Zeng, M.S. Whittingham, C.P. Grey, *Chem. Mater.* 24 (2012) 2952–2964.
- [26] J. Mao, K. Dai, Y. Zhai, *Electrochim. Acta* 63 (2012) 381–390.
- [27] J.-H. Kim, N.P.W. Pieczonka, Z. Li, Y. Wu, S. Harris, B.R. Powell, *Electrochim. Acta* 90 (2013) 556–562.
- [28] X. Fang, N. Ding, X.Y. Feng, Y. Lu, C.H. Chen, *Electrochim. Acta* 54 (2009) 7471–7475.
- [29] T. Aoshima, K. Okahara, C. Kiyohara, K. Shizuka, *J. Power Sources* 97–98 (2001) 377–380.
- [30] D.H. Jang, Y.J. Shin, S.M. Oh, *J. Electrochem. Soc.* 143 (1996) 2204–2211.
- [31] N. Armandi, K. Zaghib, F. Gendron, A. Mauger, C.M. Julien, *J. Magn. Magn. Mater.* 309 (2007) 100–105.
- [32] J.J. Jia, T.A. Calcott, J. Yurkas, A.W. Ellis, F.J. Himpel, M.G. Samant, J. Stohr, D.L. Ederer, J.A. Carlisle, E.A. Hudson, L.J. Terminello, D.K. Shuh, R.C.C. Perera, *Rev. Sci. Instrum.* 66 (1995) 1394–1397.
- [33] G.Q. Liu, L. Wen, Y.M. Liu, *J. Solid State Electrochem.* 14 (2010) 2191–2202.
- [34] B. Hai, A.K. Shukla, H. Duncan, G. Chen, *J. Mater. Chem. A* 1 (2013) 759–769.
- [35] H. Xia, S.B. Tang, L. Lu, Y.S. Meng, G. Ceder, *Electrochim. Acta* 52 (2007) 2822–2828.
- [36] Z. Chen, S. Qiu, Y. Cao, X. Ai, K. Xie, X. Hong, H. Yang, *J. Mater. Chem.* 22 (2012) 17768–17772.
- [37] H.M. Wu, I. Belharouak, A. Abouimrane, Y.K. Sun, K. Amine, *J. Power Sources* 195 (2010) 2909–2913.
- [38] W. Yang, X. Liu, R. Qiao, P. Olalde-Velasco, J.D. Spear, L. Roseguo, J.X. Pepper, Y.-d. Chuang, J.D. Denlinger, Z. Hussain, *J. Electron Spectrosc. Relat. Phenom.* 190 (2013) 64–74.
- [39] F. de Groot, A. Kotani, *Core Level Spectroscopy of Solids*, CRC Press Taylor & Francis Group, Boca Raton, 2008.
- [40] X. Liu, J. Liu, R. Qiao, Y. Yu, H. Li, L. Suo, Y.-s. Hu, Y.-D. Chuang, G. Shu, F. Chou, T.-C. Weng, D. Nordlund, D. Sokaras, Y.J. Wang, H. Lin, B. Barbiellini, A. Bansil, X. Song, Z. Liu, S. Yan, G. Liu, S. Qiao, T.J. Richardson, D. Prendergast, Z. Hussain, F.M.F. de Groot, W. Yang, *J. Am. Chem. Soc.* 134 (2012) 13708–13715.
- [41] X. Liu, D. Wang, G. Liu, V. Srinivasan, Z. Liu, Z. Hussain, W. Yang, *Nat. Commun.* 4 (2013) 2568.
- [42] R. Qiao, T. Chin, S.J. Harris, S. Yan, W. Yang, *Curr. Appl. Phys.* 13 (2013) 544–548.
- [43] A.J. Achkar, T.Z. Regier, H. Wadati, Y.J. Kim, H. Zhang, D.G. Hawthorn, *Phys. Rev. B* 83 (2011) 081106.
- [44] W.-S. Yoon, M. Balasubramanian, K.Y. Chung, X.-Q. Yang, J. McBreen, C.P. Grey, D.A. Fischer, *J. Am. Chem. Soc.* 127 (2005) 17479–17487.
- [45] P. Olalde-Velasco, J. Jiménez-Mier, J.D. Denlinger, Z. Hussain, W.L. Yang, *Phys. Rev. B* 83 (2011) 241102.
- [46] W.-S. Yoon, K.-Y. Chung, K.-H. Oh, K.-B. Kim, *J. Power Sources* 119–121 (2003) 706–709.
- [47] M.M. Thackeray, Y. Shao-Horn, A.J. Kahaian, K.D. Kepler, E. Skinner, J.T. Vaughan, S.A. Hackney, *Electrochim. Solid-State Lett.* 1 (1998) 7–9.
- [48] G. Pistoia, A. Antonini, R. Rosati, D. Zane, *Electrochim. Acta* 41 (1996) 2683–2689.
- [49] T. Eriksson, A.M. Andersson, A.G. Bishop, C. Gejke, T. Gustafsson, J.O. Thomas, *J. Electrochem. Soc.* 149 (2002) A69–A78.
- [50] D. Aurbach, B. Markovsky, G. Salitra, E. Markevich, Y. Talyossef, M. Koltypin, L. Nazar, B. Ellis, D. Kovacheva, *J. Power Sources* 165 (2007) 491–499.
- [51] L. Yang, B. Ravdel, B.L. Lucht, *Electrochim. Solid-State Lett.* 13 (2010) A95–A97.